

**Eric T. DeShong<sup>1</sup>**

Department of Mechanical Engineering,  
Pennsylvania State University,  
3127 Research Drive,  
State College, PA 16801  
e-mail: etd5060@psu.edu

**Reid A. Berdanier**

Department of Mechanical Engineering,  
Pennsylvania State University,  
3127 Research Drive,  
State College, PA 16801  
e-mail: rberdanier@psu.edu

**Karen A. Thole**

Department of Mechanical Engineering,  
Pennsylvania State University,  
3127 Research Drive,  
State College, PA 16801  
e-mail: kthole@psu.edu

# Predictive Modeling of Local Film-Cooling Flow on a Turbine Rotor Blade

*In the turbine section of a modern gas turbine engine, components exposed to the main gas path flow rely on cooling air to maintain hardware durability targets. Therefore, monitoring turbine cooling flow is essential to the diagnostic and prognostic efficacy of a condition-based operation and maintenance (CBOM) approach. This study supports CBOM goals by leveraging supervised machine learning to estimate relative changes to local film-cooling flowrate using surface temperature measured on the pressure side of a rotating turbine blade operating at engine-relevant aerothermal conditions. Throughout the lifetime of a film-cooled turbine component, characteristics of the film-cooling flow—such as film trajectory and cooling effectiveness—vary as degradation-driven geometry distortions occur, which ultimately affects the relationship between the model input and the model output—film-cooling flowrate predictions. The present study addresses this complication by testing a data-driven model on multiple turbine blades of the same nominal design, but with each blade exhibiting different localized film-cooling flow characteristics. By testing the model in this manner, strategies for mitigating the detrimental effects of film-cooling flow characteristic variations on model performance were investigated, and the corresponding flowrate prediction accuracy was quantified. [DOI: 10.1115/1.4055972]*

**Keyword:** heat transfer and film cooling

## 1 Introduction

In pursuit of maximizing thermodynamic efficiency, the firing temperature of modern gas turbine engines can exceed 1600 °C (2900 °F) in certain applications [1]. To prevent damage caused by the high-temperature main gas path (MGP) flow, turbine components are often highly cooled using a combination of internal and external methods. The result of these various cooling schemes is overall cooling effectiveness of approximately 60% for modern airfoils [2], which shows the critical role that cooling flows play in enabling the safe operation of gas turbine hardware.

When cooling flow decreases, there is an associated increase in hardware temperatures. In the hottest sections of the engine, such as the combustor and first-stage turbine sections, increased hardware temperatures accelerate the mechanisms by which hardware failures often occur: high cycle fatigue, oxidation, sulfidation, hot corrosion, creep, erosion [3], and thermal barrier coating spallation.

To monitor degradation and minimize associated repair costs, condition-based operation and maintenance (CBOM) has become the ideal strategy for gas turbine engine maintenance. In fact, a consensus report published by the National Academies' Division on Engineering and Physical Sciences identified CBOM as a high-priority research area for the improvement of gas turbine engines [4]. The number of sensors installed on engines has expanded over time, so too has the potential condition-monitoring methods available for improving CBOM. For example, blade tip timing [5], fast-response pressure [6–8], and temperature [9] sensors have been applied to monitor certain components and regions of the engine.

In the turbine section, the application of infrared (IR) thermography for monitoring hardware temperatures is becoming increasingly widespread. In land-based applications, where space and weight factors are less restrictive, IR thermography has already shown

the capability for long-term engine integration on the order of 8000 engine hours [10]. For aviation engines, IR camera integration and high-quality blade temperature imaging were shown by Markham et al. [11]. While continuous IR camera integration is likely not yet feasible for on-wing installations, discrete monitoring via tarmac inspection between flights may be viable. Given the relatively untapped potential of IR thermography for component monitoring in gas turbine engines, this study demonstrates method development for applying an IR camera to the monitoring of local blade coolant flowrate—a parameter for which there are currently no established monitoring techniques.

## 2 Literature Review

As cooled turbine components are operated over their lifetime, a number of phenomena can affect their film-cooling performance. Prior to operation, hole manufacturing [12] and thermal barrier coating (TBC) application processes [13] can cause various geometrical distortions of the nominal film-cooling hole design. During operation, the primary drivers of hole surface distortion are oxidation and deposition, with secondary drivers being corrosion, erosion, and foreign object damage [14]. The present study focuses on the prediction of changes to film-cooling flowrate from some nominal condition; as a result, only the effects of TBC and particulate deposition blockages will be considered because these hole degradation mechanisms lead to reduced film-cooling flowrate (for a constant pressure ratio). Furthermore, because the present study uses diffuser-shaped film-cooling holes, special attention is directed to studies examining holes of similar design.

The geometric implications of TBC and particulate deposition are very similar in regard to film-cooling holes; the majority of accumulation occurs at the hole exit with some additional accumulation extending into the hole [13–16]. This form of blockage leads to a reduction in the hole exit area, which in turn has a number of implications on the performance of the film-cooling hole. The relationship between the pressure ratio across the hole and the blowing ratio is fundamentally altered—the blowing ratio is decreased at an equivalent pressure ratio [13]. Although the blowing ratio is

<sup>1</sup>Corresponding author.

Contributed by the International Gas Turbine Institute (IGTI) of ASME for publication in the Journal of Turbomachinery. Manuscript received August 20, 2022; final manuscript received October 9, 2022; published online November 7, 2022. Tech. Editor: David G. Bogard.

decreased, the exit area reduction causes an associated increase in jet velocity, resulting in a conservation of momentum flux ratio ( $\rho_h U_h^2 / \rho_{MGP} U_{MGP}^2$ ) [14]. These flow differences affect both the area-averaged and local performance of the film cooling, as evidenced by adiabatic effectiveness measurements.

Multiple studies have reported adiabatic film-cooling effectiveness results for partially blocked holes. Bunker [14] reported a near hole ( $x/D < 20$ ) reduction in laterally-averaged film-cooling effectiveness of 30% for diffuser-shaped holes with a 15% exit area reduction. Another study from Sundaram and Thole [17] investigated a row of vane endwall film-cooling holes and found a 25% reduction in the exit area of a single hole caused a 10% reduction in area-averaged adiabatic effectiveness. It is worth noting that these results were observed for a cylindrical hole shape.

Wang et al. [16] reported a 34% reduction in area-averaged adiabatic effectiveness for a 20% hole blockage. Perhaps, the most comprehensive set of results was reported by Whitfield et al. [13], who studied multiple exit area reductions, hole shapes, density ratios, pressure ratios, and blowing ratios. Their results indicated that the percent reduction of area-averaged effectiveness for all cases collapsed onto a single curve when measurements were analyzed as a function of the corrected momentum flux ratio. In general, these studies cumulatively show a strong detriment to area-averaged adiabatic effectiveness when hole exit blockage occurs.

In addition to these area-averaged effectiveness trends, the variations in downstream effectiveness distribution are also important to consider. Wang et al. [16] found that a hole exit blockage resulted in a stronger counter-rotating vortex pair, which caused an associated decrease to film effectiveness and coolant coverage. Decreased coolant coverage was also observed by Whitfield et al. [13]. Specifically, when comparing a partially blocked hole to an unblocked hole at an equivalent blowing ratio, the partially blocked hole exhibited further downstream propagation of low centerline effectiveness, but with a narrowing effect that diminished film coverage.

However, the commonalities in these studies lead to two basic conclusions. First, decreased area-averaged film-cooling performance is expected when hole blockage occurs. Second, even for equivalent blowing ratios, the presence of a blockage will change the effectiveness contours relative to the unblocked case. The interaction of these two conclusions, along with the myriad of additional parameters influencing blade cooling effectiveness distribution, creates a challenge for predictive modeling of blade film-cooling

flow variations. The present study addresses this challenge by developing a data-driven film-cooling flow prediction model that maintains high accuracy as degradation-driven changes to cooling effectiveness distribution occur. This unique approach has not been previously reported in the literature and opens many possibilities for CBOM.

### 3 Experimental Methods

Experiments for this study were performed at the Steady Thermal Aero Research Turbine (START) Laboratory. The facility was introduced in detail by Barringer et al. [18], and a shortened description is given here.

**3.1 Test Facility Description.** The START test turbine is integrated within an open-loop continuous-duration facility that operates at engine-relevant aerothermal conditions. A facility-level view is shown in Fig. 1 with major components highlighted. The colored flow arrows indicate the direction and relative temperature of the flow.

Two large compressors (1.1 MW, 1500 hp) draw ambient air into the system and pressurize the flow to approximately 480 kPa (70 psia) at a maximum combined mass flowrate of 10.4 kg/s (25 lb<sub>m</sub>/s). This pressurization causes an associated temperature increase up to a nominal compressor exit temperature of 110 °C (230 °F). Flow exiting the compressors is split into two streams: the MGP and cooling streams. The MGP flow progresses through an in-line natural gas combustion chamber, which provides temperature control of the flow prior to its entrance to the test section. At the nominal MGP flowrate, the combustor can achieve temperatures up to 400 °C (750 °F), although MGP temperatures were lower in this particular study. Table 1 presents various nondimensional parameters for the turbine operating point used in this study.

The coolant stream bypasses the combustion chamber and instead passes through a shell-and-tube heat exchanger to bring its temperature down to 0 °C (32 °F). The facility has the capability to independently control three turbine cooling and sealing flows: purge flow, vane trailing edge flow, and blade coolant flow. In this study, the purge and vane trailing edge flows were held constant, while the blade coolant flow ( $\dot{m}_c$ ) was varied between four mass flowrate set points.

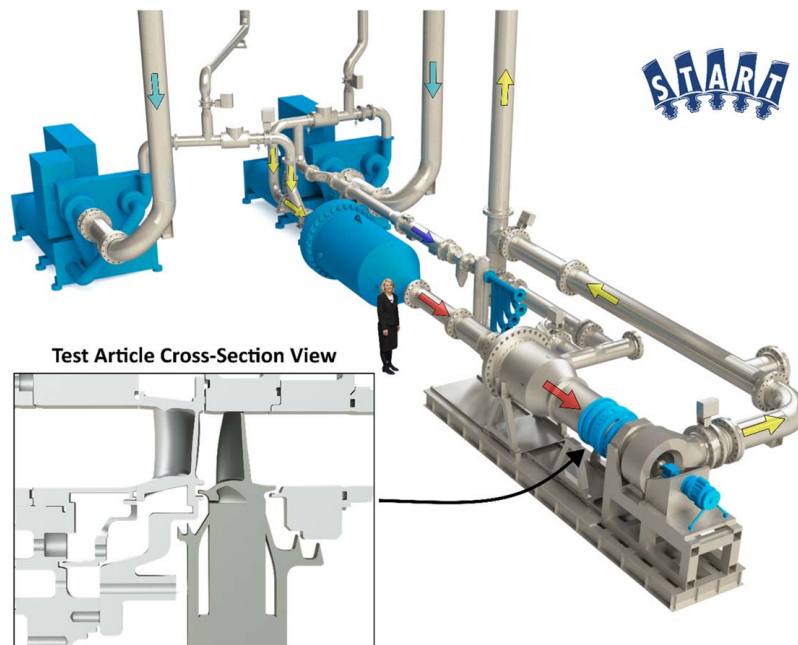


Fig. 1 START laboratory facility view

**Table 1 Turbine operation non-dimensional parameters**

Parameter	Value
Vane inlet Mach number	0.1
Vane inlet axial Reynolds number	$8.8 \times 10^4$
Blade inlet axial Reynolds number	$8.6 \times 10^4$
Rotational Reynolds number	$2.7 \times 10^6$
Density ratio, $\rho_P/\rho_{MGP}$	1.7

These MGP and coolant flows reconvene in the turbine test section, which is shown in Fig. 2 with relevant instrumentation labels. The main diagnostic measurement collected in this study was the blade surface temperature (not shown in Fig. 2), so it was important to control the flowrate and temperature of the MGP and blade cooling flows. The MGP flowrate and temperature were held constant, and measurements were collected upstream of the test section. Specifically, the MGP flowrate was measured using a Venturi flowmeter upstream of the turbine stage, and MGP temperature was measured by six circumferentially distributed thermocouple probes located at the midspan upstream of the vane. Similarly, blade coolant flowrate was measured using a Venturi flowmeter upstream of the test section, and the temperature was measured using four circumferentially distributed thermocouple probes positioned just before the pre-swirler vanes, which prepare the blade coolant for injection to the rotor assembly.

The rotor blades used in this study are representative of a modern first-stage high-pressure turbine blade with complex internal and external cooling features. The cooling flow enters the blades through the disk attachment and subsequently progresses through internal passageways before exiting film-cooling holes on the pressure-side surface. The resulting blade surface temperature distribution was measured using an IR camera system. The calibration, integration, operation, and post-processing methods used with the IR camera were described in detail by Knisely et al. [19], and an abbreviated description is provided here.

**3.2 Infrared Imaging Methods.** The IR camera used in this study measures radiant energy in the long wave IR spectrum ( $8 \mu\text{m} < \lambda < 15 \mu\text{m}$ ). The calibration of the IR detector was performed using a calibration plate at a range of surface temperatures, following the process detailed by Mori et al. [20]. The camera optics were integrated into a probe installed through an additively manufactured vane, as shown in Fig. 3(a). The vane featured a cutout along the suction side to allow optical access to the blades. The camera image collection was phase-locked to the rotor revolution, which enabled consistent imaging of the single cooling hole shown in Fig. 3(a).

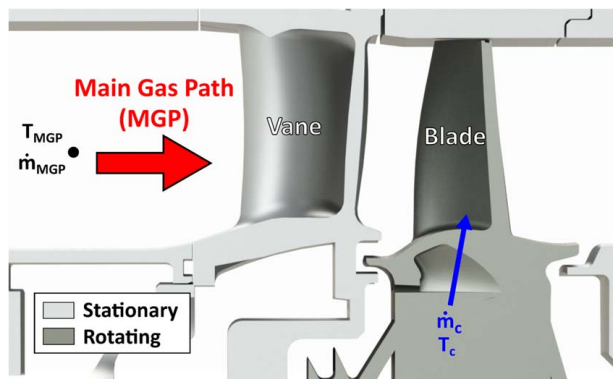


**Fig. 2 Representative cross-sectional view of the one-stage turbine test article with relevant flows labelled**

Prior to testing, a high emissivity coating with an emissivity of 0.92 was applied to the blades. During data collection, the camera was operated with an integration time of  $2 \mu\text{s}$ , which minimized the combined effects of image blur and spatial noise for the particular turbine rotating speed in this experiment [19]. To further reduce measurement noise, 200 consecutive images were collected and subsequently averaged. Finally, the images were post-processed using binning and  $3 \times 3$  median filterings, which reduced measurement errors associated with striping and nonresponsive pixels [19]. Figure 3(b) shows an example thermal image—expressed in terms of overall cooling effectiveness ( $\phi$ )—that results from these processes. The overall effectiveness was computed using Eq. (1)

$$\phi = \frac{T_{MGP} - T_s}{T_{MGP} - T_c} \quad (1)$$

where  $T_{MGP}$ ,  $T_c$ , and  $T_s$  are the main gas path, coolant, and surface temperatures, respectively.

The marker in Fig. 3(b) indicates the approximate location of the lower left edge of the cooling hole, and the dashed line marks the trajectory of the line of maximum effectiveness, which is assumed to indicate the film-coolant trajectory along the blade surface. The method of determining the location of these features was initially introduced by Knisely et al. [21], and a shortened description is provided here.

First, the maximum effectiveness at all  $x$  locations was determined to identify the coolant trajectory. A moving average filter was applied to the identified trajectory to capture the migration of the coolant while suppressing the  $z$ -direction variability caused by pixel-to-pixel variability. Then, the edge location of the cooling hole was identified by the point of maximum slope in effectiveness along the line of maximum effectiveness. In Fig. 3(b), the segment of the line of maximum effectiveness upstream of the cooling hole

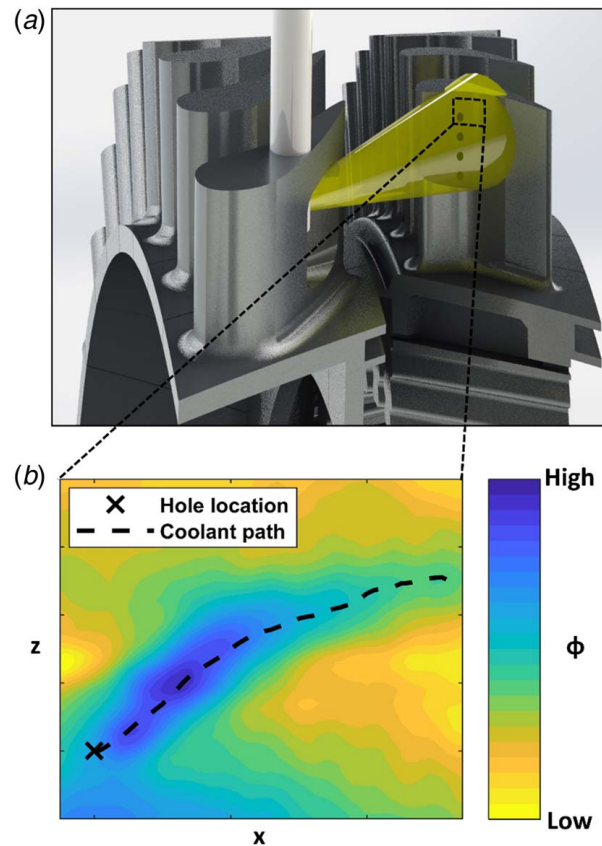


**Fig. 3 IR camera (a) integration and blade view and (b) overall effectiveness contour corresponding to the training blade at the nominal bulk blade cooling flowrate condition**



was removed for clarity. Critically, this method of identifying a common location for all blade cooling holes and coolant trajectories is both objective and repeatable, which is important for establishing consistency on a case-by-case basis.

**3.3 Training and Test Cases.** This study utilizes a data-driven approach to generate a model that takes inputs of overall effectiveness and outputs predictions of single-hole blade coolant flowrate. The flowrate predictions extend the usefulness of an engine-integrated IR camera by contributing to root cause analysis of blade degradation and high-temperature blade failures. As dictated by the data-driven approach, data were separated into training and testing sets. The training data were collected exclusively for a single film-cooling hole on a single blade. The testing data consist of four cases: one case using the same blade as the training data (B1), and three cases using different blades (B2, B3, and B4). For brevity, the test cases will be referred to by the blade they represent (e.g., “B1”). Each test case exhibits variations in overall effectiveness distribution, which are analogous to the variations caused by degraded film-cooling holes. With this training and testing setup, this study is leveraging blade-to-blade manufacturing variations [21] as a method for simulating film-cooling degradation over time.

To quantify the differences between the training and testing data, the single-hole flow parameter and coolant trajectory differences were computed. Using a benchtop flow rig, the flow parameter (FP) was calculated using Eq. (2)

$$FP = \frac{\dot{m}_h \sqrt{T_{in}}}{P_{out}} \left[ \frac{\text{kg} \sqrt{\text{K}}}{\text{Pa} \cdot \text{s}} \right] \quad (2)$$

where  $\dot{m}_h$  is the single-hole mass flowrate,  $T_{in}$  is the inlet temperature boundary condition measured just upstream of the blade root, and  $P_{out}$  is the ambient room pressure boundary condition. Note that the flow parameter measurements were collected using a benchtop flow rig, so flow parameter measurements for each blade were collected across a range of pressure ratios, with pressure ratio calculated according to Eq. (3)

$$PR = \frac{P_{in}}{P_{out}} \quad (3)$$

Importantly, the blade-to-blade ratio between the measured flow parameter values is consistent across all pressure ratios, meaning flow comparisons between each blade can be expressed as a single constant value. Furthermore, at equivalent pressure and temperature boundary conditions, the flow parameter ratio is equivalent to the ratio of single-hole film-cooling mass flowrates. The FP uncertainty, which is a function of  $\dot{m}_h$ ,  $T_{in}$ , and  $P_{out}$ , nondimensionalized by the FP of the training case ( $FP_0$ ) is equal to 2.35% [21].

Coolant trajectory differences with respect to the training case were quantified using the  $z$ -axis offset between each trajectory. The  $z$ -offset was nondimensionalized by the hole diameter ( $D$ ), such that trajectory differences can be interpreted by the number of hole diameters of offset. In Fig. 4, this difference is shown at a single  $x/D$  location for the training blade and B4 trajectories corresponding to the nominal bulk blade flowrate condition ( $\dot{m}_{c,nom}$ ). By computing the root-mean-square (RMS) of the path differences at all  $x/D$  locations, a single path difference value for each blade was curated. Similarly, the uncertainty in the coolant path identification was determined by computing the RMS difference between the smoothed and un-smoothed lines of maximum effectiveness. This method returns a different uncertainty for each case, with the minimum uncertainty occurring for B3 at 0.21 hole diameters and the maximum uncertainty occurring for B4 at 0.52 hole diameters.

The flow parameter and trajectory differences between the training and testing blades are shown in Fig. 5. The non-hatched bars correspond to the left ordinate, which expresses FP as a percentage difference with respect to the training case. For example, a bar height of 25% indicates the test blade exhibits a 25% increase in

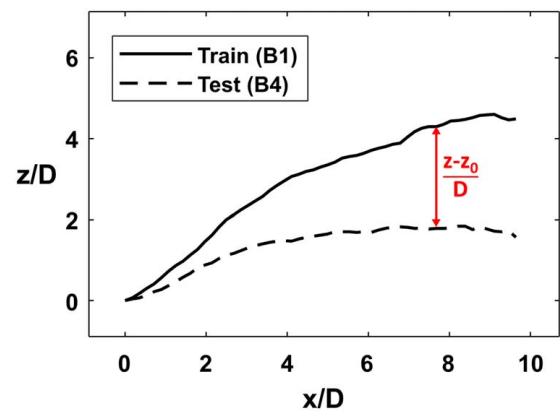


**Fig. 4 Z-Offset between the training blade (B1) and B4 coolant trajectories**

flow parameters relative to the training blade. The hatched bars correspond to the right ordinate, which shows the nondimensional coolant trajectory variation relative to the training blade.

The B1 test case examines the same blade as the training blade, which is why its FP difference in Fig. 5 is equal to zero. Although not comprehensive, testing the model on a second data set collected for the same blade provides information regarding model stability. Despite the flow parameter equivalence, a coolant trajectory offset of 0.26 hole diameters was observed, as indicated by the blue hatched bar in Fig. 5.

The B2 test case introduces a new blade to the analysis with minimal changes to flow parameters and coolant trajectory. The flow parameter is within 4% of the training blade, and the coolant trajectory is only 0.33 hole diameters offset from the training blade.

The B3 test case introduces a more substantial flow parameter difference, while still exhibiting a similar coolant trajectory. For this case, the flow parameter was increased by 18%, but the coolant trajectory is still within 0.50 hole diameters of the training blade. Although perhaps less common than the decreased flow scenario, this case enables the investigation of model accuracy when film-cooling flowrate increases as a result of degradation—a phenomenon that can occur from excessive blade erosion [14] or when deposits liberate from the blade and peel-off a section of TBC [17] at the hole exit.

Finally, the B4 test case represents a heavily distorted film-cooling hole, with a flow parameter decrease of nearly 50%. This decrease in flow parameter dictates that, for the same pressure and temperature boundary conditions, the B4 cooling hole flows only half as much compared to the training blade. This substantial decrease in flowrate is accompanied by a heavily-modified coolant trajectory of nearly two hole diameters.

In addition to the differences identified for flow parameters and coolant trajectory, the test cases also exhibit local changes to overall cooling effectiveness. To quantify these changes, the pitchwise effectiveness profile at  $x/D = 2$  was compared between the training and test cases. Definitions of the parameters used to compare the profiles are shown in Fig. 6 with respect to an average effectiveness profile. The peak-to-trough effectiveness amplitude ( $A$ ) was calculated between the local minimum and maximum effectiveness, and the peak width ( $W$ ) was determined based on the peak width at  $A/2$ . In addition to these two parameters, pitchwise-averaged cooling effectiveness ( $\bar{\phi}$ ) was also computed.

These three parameters are compared in Fig. 7 relative to the training case ( $\phi_0$ ,  $A_0$ , and  $W_0$ ). The relative bar heights between each test case are different in each plot, which shows the uniqueness of each case. As expected, B1 results are most similar to the training case because the geometry has not changed. Additionally, the substantial flow decrease through the hole on B4 has resulted in corresponding reductions of  $\bar{\phi}$  and  $A$ , as would be expected. Interestingly, B2 and B3 exhibit increased  $A$  and  $W$  relative to the

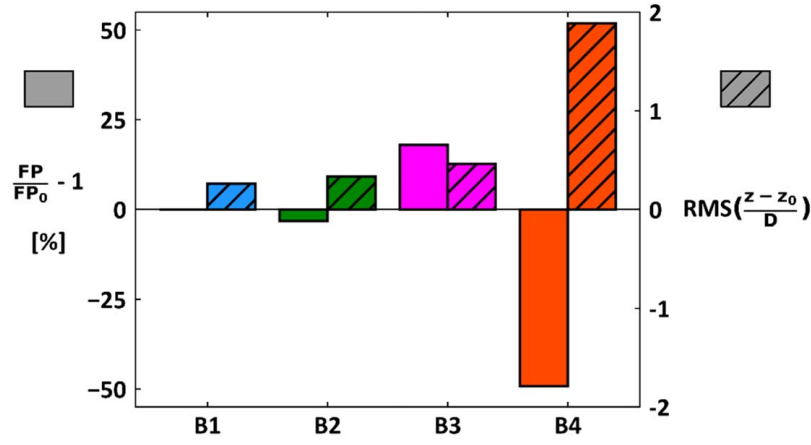


Fig. 5 Flow parameter (solid bars) and coolant trajectory (hatched bars) differences between the training and testing blades

training case, yet their  $\bar{\phi}$  values are relatively low. It is these noted differences that, along with coolant trajectory variations, create the difficulty in relating inputs of cooling effectiveness to flow parameters.

Thus far, all results have been presented for the nominal bulk blade coolant flowrate. To provide an additional variation to single-hole flowrates, the bulk blade coolant flowrate boundary condition was varied to three additional set points. The effects of bulk flow changes were combined with the flow parameter variations noted in Fig. 5 to compute the single-hole mass flowrate using Eq. (4)

$$\frac{\dot{m}_h}{\dot{m}_{h,0,nom}} = \left( \frac{FP}{FP_0} \right) \left( \frac{\dot{m}_c}{\dot{m}_{c,nom}} \right) \quad (4)$$

where  $\dot{m}_{h,0,nom}$  is the training blade single-hole flowrate corresponding to the  $\dot{m}_{c,nom}$  bulk flow condition. Equation (4) was generated by assuming that a film-cooled blade acts similarly to a simple manifold system, meaning any changes to bulk blade coolant flowrate results in a proportional change to single-hole flowrate [22]. The computed single-hole flowrates are presented in Fig. 8 for all cases.

Figure 8 shows that only the B1 and B2 single-hole flowrates fall almost entirely within the training data range. The highest two flowrates for B3 and the lowest three flowrates for B4 represent extrapolations of the model above and below the training range, respectively. These data enable the analysis of accuracy detriments associated with model extrapolation. Altogether, the flowrate and overall cooling effectiveness variations captured in the test cases provide a diverse set of data that facilitates the investigation of

techniques for accurate predictive modeling in the presence of various degrees of hole degradation.

**3.4 Modeling Approaches.** The two approaches used to generate the predictive models are described in this section. First, the Baseline (BL) modeling approach is explained and the associated feature selection is shown. Second, a modified approach—the Coolant-Relative (CR) modeling approach—is introduced and effects on feature selection are shown relative to the BL model. The BL modeling approach was first introduced by DeShong et al. [23], and the process implemented here is nearly identical. Any deviations from the original process are noted.

**3.5 Baseline Model.** In the BL modeling approach, a rectangular domain encompassing the target film-cooling hole and coolant trajectory was utilized. This domain is shown in Fig. 9 for the training case at the nominal bulk blade coolant flowrate.

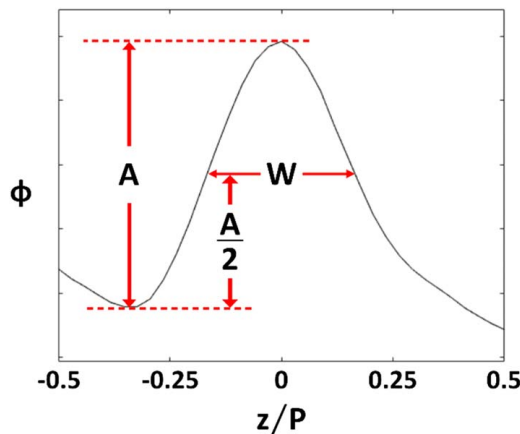


Fig. 6 Definitions of the parameters used to characterize the overall effectiveness profiles at  $x/D = 2$

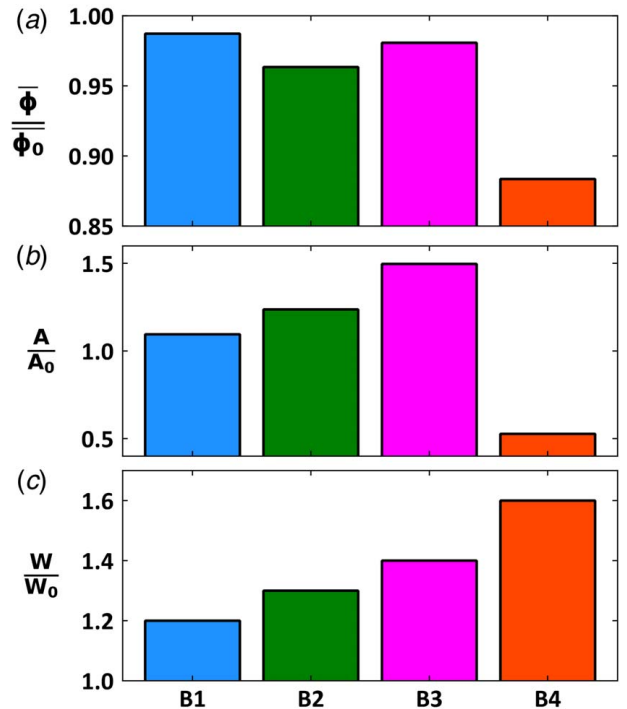
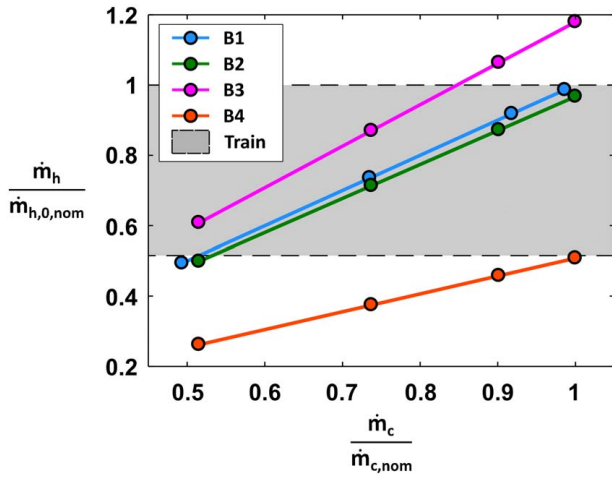


Fig. 7 Effectiveness profile quantification of (a) laterally-averaged effectiveness, (b) peak-to-trough effectiveness amplitude, and (c) peak effectiveness width at  $x/D = 2$



**Fig. 8** Calculated single-hole flowrate variations for all training and testing cases. The abscissa shows the bulk blade coolant flowrate set points, and the ordinate shows the resulting single-hole flowrates, both nondimensionalized by the nominal value.

For consistency, the size and position of this rectangular domain relative to the identified cooling hole location were held constant across all training and testing cases. The cooling effectiveness values corresponding to each pixel within this domain comprise the set of candidate features that may be used for modeling.

This baseline modeling approach contains only two differences with respect to the process introduced by DeShong et al. [23]. First, a single cooling hole was isolated, whereas DeShong et al. isolated a larger domain consisting of four cooling holes. The four-hole domain could lead to prediction errors if single-hole flowrate variations are not consistent between each hole in the domain. For this reason, the current study examines only a single hole. Second, model inputs of cooling effectiveness were used in this study, as opposed to blade surface temperature. This change was made to account for the effects of case-to-case  $T_{MGP}$  and  $T_c$  variations—a process that was previously accomplished via the inclusion of covariate parameters in the data-driven model.

The candidate feature set—the entire set of features sourced from the IR images—was passed to LASSO (Least Absolute Shrinkage and Selection Operator) for regularized regression [24] to generate the model for predicting film-cooling flow variations. The optimization equation for LASSO is shown in Eq. (5)

$$\min_{\beta_0, \beta} \frac{1}{2n} \sum_{i=1}^n \left[ \left( \frac{FP}{FP_0} \right)_{meas,i} - \beta_0 - \Phi_i^T \beta \right]^2 + \alpha \beta_1 \quad (5)$$

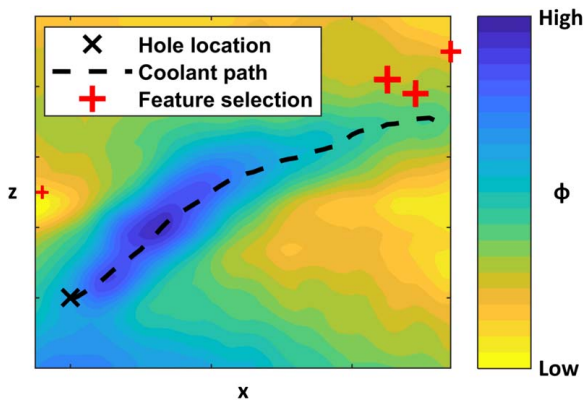


**Fig. 9** BL model feature selection shown relative to cooling effectiveness contours for the training case at the nominal bulk blade coolant flowrate

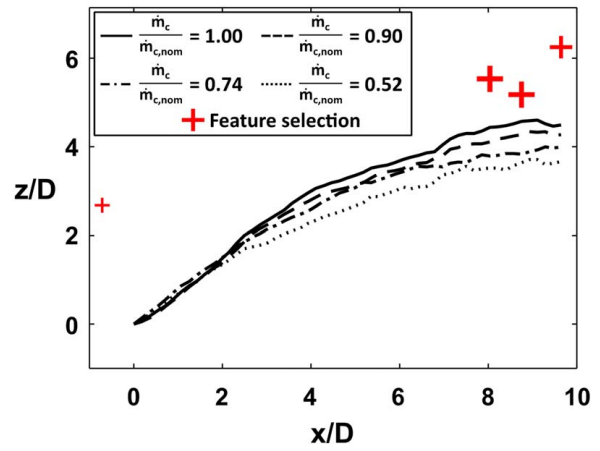


**Fig. 10** Comparison of feature selection locations relative to coolant trajectories in the training data set

where  $\left( \frac{FP}{FP_0} \right)_{meas,i}$  is the  $i$ th measured flow parameter ratio,  $\Phi_i$  is the

$i$ th set of features,  $n$  is the number of training cases ( $n=4$ ),  $\alpha$  is the tuning parameter, and  $\beta$  is the set of model coefficients. Note that  $\beta_0$  is simply the offset term in the linear model and therefore does not specifically apply to the training case. Through the minimization of Eq. (5), the model coefficients are identified by their ability to reduce the sum-squared-error relative to the flow parameter ratio measurements. This process is modified by the second term in Eq. (5)—often referred to as the penalty term—which increases as the magnitude of the coefficients increase. In doing so, the second term causes the optimization process to return lower coefficient values, with some coefficients shrinking to zero. Due to the large size of the candidate feature set in this study consisting of about 3000 features, this shrinkage capability of LASSO—which effectively eliminates less informative features—was advantageous for minimizing the number of features in the model. The extent of regularization (prevention of overfitting) and feature selection is determined by the numerical value of the tuning parameter ( $\alpha$ ). The tuning parameter ( $\alpha$ ) was determined objectively using the K-fold cross-validation technique, which selects the optimal  $\alpha$  that reduces overfitting across the entire training data set.

The four features selected by LASSO are shown in Fig. 9 by the markers. The markers are sized relative to their corresponding coefficients in the model, meaning the largest markers correspond to the most influential features. There are two main observations from Fig. 9. First, the feature selection is fairly sparse with only four selected features. This result is consistent with DeShong et al. [23], which showed accurate predictions could be obtained from models with as few as four features. Second, the two most important features lie just above the line of maximum effectiveness, relatively far downstream of the film-cooling hole. To understand why these features were selected, Fig. 10 shows the feature selection relative to the coolant trajectories for each flowrate included in the training set.

Figure 10 shows that as the coolant flowrate is decreased, the coolant jet trajectory exhibits less  $z$ -direction propagation. This effect is likely due to the decreasing momentum flux ratio between the film-cooling and MGP flows, which causes the coolant to be more easily swept in the direction of the MGP flow (along the  $x$ -direction). It is this variation in the coolant trajectories that causes the two most influential features in Fig. 9 to stand out from the rest of the features in the candidate feature set. As the trajectory in the  $z$ -direction decreases for the cooling jet, the spacing between the selected features and the point of maximum effectiveness increases. This relative motion causes the selected feature to “fall down” the cooling effectiveness profile, as illustrated in Fig. 11. This effect provides a secondary mechanism by which cooling effectiveness decreases with film-cooling flowrate, which

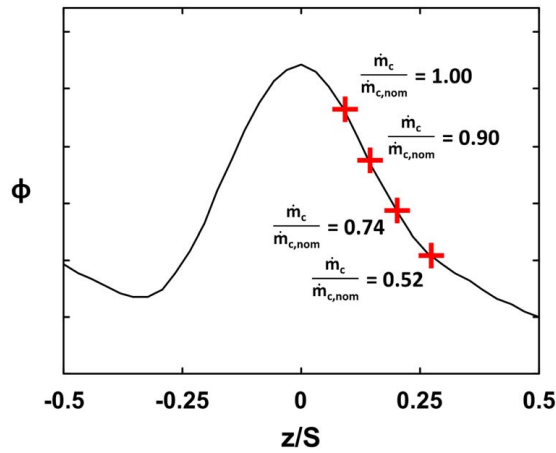


Fig. 11 Example positioning of a single selected feature relative to the typical cooling effectiveness profile

supplements the primary effect of an area-averaged decrease in effectiveness as flowrate decreases.

The BL model trained in this section was applied to the test cases to generate film-cooling flowrate predictions. The accuracy of these predictions will be compared with the CR model in the Prediction Results section of the paper.

**3.6 Coolant-Relative Modeling Approach.** The goal of the CR modeling approach is to define candidate features relative to the line of maximum effectiveness to maintain their relative positioning across all cases. The hypothesis is that, by defining the features in this way, the model accuracy will be improved for cases that have deviated greatly from the training data. To accomplish this goal, the feature domain was redefined using the identified coolant trajectory as a datum. As shown in Fig. 12, features within  $\pm 0.5$  pitch of the coolant trajectory were included in the domain. The features outside of this single pitch domain were not included in the set of candidate features.

While this method accounts for case-to-case variations in coolant trajectory, the additional differences noted in Fig. 7 are still present. Critically, any discrepancies in effectiveness peak locations ( $W$ ) between the training and testing cases will affect the coolant-relative positioning of selected features, similar to the effect shown in Fig. 11. Therefore, image registration, which is

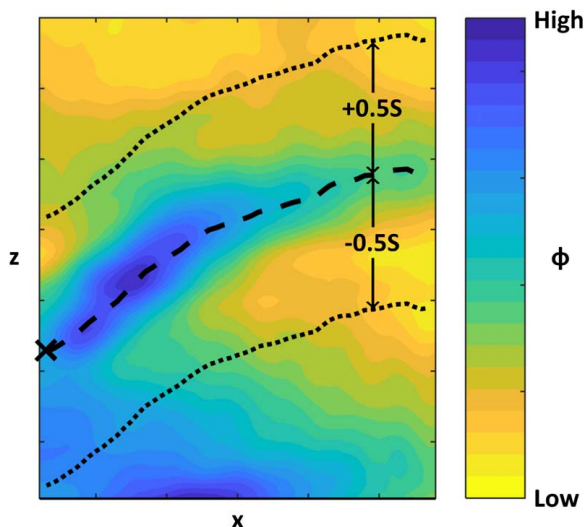


Fig. 12 CR model domain definition relative to the identified coolant trajectory

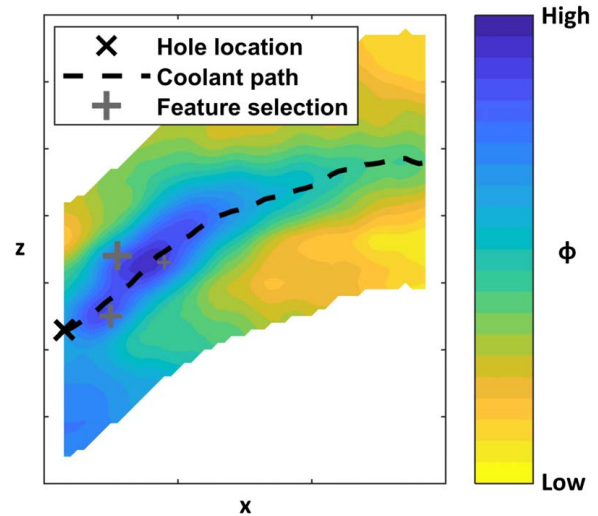


Fig. 13 CR model feature selection shown relative to the cooling effectiveness contours for the training case at the nominal blade coolant flow condition

an image processing tool that automates the alignment of similar images, was performed to adjust  $W$ , while largely maintaining  $\phi$  and  $A$ . The image registration was given the freedom to translate, rotate, scale, and shear the test set images to minimize grayscale intensity differences with respect to the training images. An added benefit of performing this registration was the correction of any errors in identifying the line of maximum effectiveness, which causes the peak effectiveness to shift away from  $z=0$  in Fig. 11. The downside of implementing this process is it extends the duration of model implementation because every image must undergo registration. However, when performed on a standard desktop computer, the registration step only added about 30 s to each image, so it does not significantly extend the overall processing time.

With this isolated and registered domain, LASSO was used to generate the predictive model and perform feature selection. The selected features are shown in Fig. 13 with respect to the training case cooling effectiveness contours at the nominal bulk blade coolant flow condition. Selected features are indicated by grey markers to differentiate them from the red markers (BL model features) shown in Fig. 9. The marker size indicates the relative magnitude of the feature coefficients in the model.

Due to the coolant-relative feature definitions used in this modeling approach, the phenomenon illustrated in Fig. 10 was not present. For this reason, the feature selection for the CR model is very different from the BL model, with selected features located near the cooling hole. This feature selection is qualitatively similar to the selection shown by DeShong et al. [23] when only the features most correlated with blade coolant flowrate are considered. Additionally, the CR model uses one less feature than the BL model, although this difference is fairly insignificant when considering both selected feature sets are a sparse down-selection of the much larger candidate feature sets.

To highlight the differences between the CR features relative to the BL features, both sets of features are shown relative to the B4 coolant trajectories in Fig. 14. B4 was chosen because it exhibits the greatest coolant trajectory deviation from the training data, as quantified in Fig. 5.

Figure 14 shows the benefit of the CR features relative to the BL features for coolant trajectories that are drastically different from the training case. The CR features move with the coolant to maintain their relative positioning, while the BL features remain in the same absolute position for all bulk blade coolant flowrate conditions. For the training blade, the BL features were located near the coolant trajectories (Fig. 10), but for B4, the BL features fall



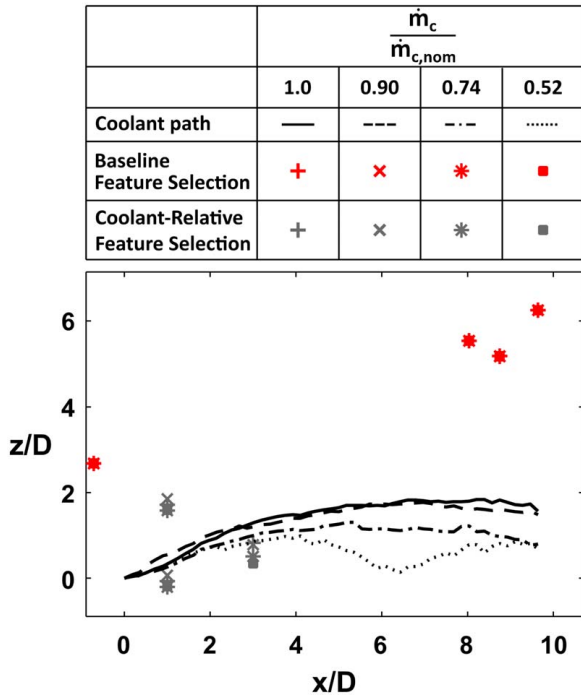


Fig. 14 BL and CR feature selection is shown relative to B4 coolant trajectories. Note that multiple marker types were not used for the BL features because their location is constant for all  $\dot{m}_c/\dot{m}_{c,nom}$  conditions.

extremely far from the coolant trajectory—about three hole diameters of separation. This discrepancy will likely cause an increased prediction error when the BL model is applied to B4.

#### 4 Prediction Results

To analyze model performance, the flow parameter predictions were compared to their corresponding flow parameter measurements to compute the error ( $E$ ). The error was quantified using Eq. (6)

$$E = \left( \frac{FP}{FP_0} \right)_{pred} - \left( \frac{FP}{FP_0} \right)_{meas} \quad (6)$$

where subscript “*pred*” indicates the predicted value, and subscript “*meas*” indicates the measured value. These error results are shown in Fig. 15 for the BL and CR models.

In Fig. 15, the bar height indicates the mean of the absolute valued error, and the range bars indicate the range of absolute value error across the four bulk blade coolant flowrate boundary conditions. The non-hatched bars (first bar in each group) correspond to the BL model, and the forward-hatched bars (second bar in each group) correspond to the CR model. The reverse-hatched bars (third bar in each group) indicate the error improvement of the CR model relative to the BL model, where a positive value indicates the CR model has outperformed the BL model, and a negative value indicates the CR model has performed worse than the BL model. Note that the flow parameter ratios in Eq. (6) are expressed as percentages, so the error in Fig. 15 represents a difference of percentages, not a percent error calculation.

As suggested by Fig. 14, B4 exhibits the largest mean prediction error for the BL model at 36%, which is over four times greater than the next highest error using the same model. When considering the CR model for this case, the prediction error was decreased to 7%—an improvement of nearly 30%. This vast improvement is attributed to the flexibility of the CR features, which allows them to conform to any coolant trajectory, as highlighted in Fig. 14. B1 also

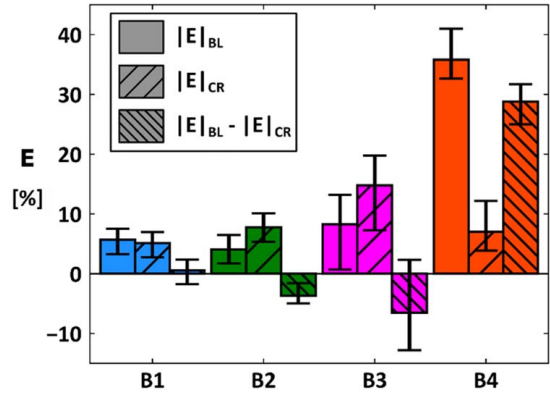


Fig. 15 Comparison of prediction errors between the BL and CR models for each test blade

exhibited a slight improvement for the CR model relative to the BL model, although this improvement was far less substantial. B2 and B3 show a slightly increased prediction error when applying the CR model, as signified by the negative heights of their reverse-hatched bars. Cumulatively, the prediction error results for B1, B2, and B3 show that the CR model may not be preferable to the BL model for cases that do not exhibit large variations in coolant trajectory. However, as degradation occurs and coolant trajectory variations become more significant, the substantial improvement noted for B4 shows that the flexibility of the CR model is necessary to minimize prediction error. To leverage the benefits of both modeling approaches, a selection could be made between the two models based on differences in the film-cooling flow relative to the training case. For example, with additional investigation, a critical trajectory offset value could be established below which the BL model would be applied, while the CR model would be reserved for the cases exhibiting greater trajectory offsets relative to the training case. Such a process would be reasonable to implement in practice given that the trajectory offsets can be sourced directly from the thermal images, meaning no additional information would be required.

#### 5 Conclusions

This study investigated approaches for data-driven modeling of single-hole film-cooling flowrate given inputs of cooling effectiveness measured on the pressure side of a highly cooled first-stage turbine rotor blade. In particular, this study focused on the effects of degradation, which was simulated using blade-to-blade manufacturing variability within a set of four blades of the same nominal design. One blade was set aside as the training case and therefore represented the zero-degradation condition. The testing cases, which consisted of the remaining three blades and one repeated data set using the training blade, represented varying levels of film-cooling hole degradation.

Using a single film-cooling hole as the target for predictive modeling, the differences in single-hole flow parameters and local cooling effectiveness were compared between the training and testing cases. The most extreme case (B4) exhibited nearly a 50% reduction in flow parameters, which caused the coolant trajectory to shift by nearly two hole diameters. Additionally, when examining the pitchwise profile of effectiveness at  $x/D = 2$ , B4 exhibited a 12% decrease in average effectiveness, a 47% decrease in peak-to-trough effectiveness variation, and a 60% increase in the width of the effectiveness peak.

With these differences quantified, two modeling approaches were applied to the testing set and single-hole flowrate predictions were generated. The first modeling approach—the Baseline Model—implemented a rectangular domain surrounding the target cooling hole to define features in absolute space. The second modeling



approach—the Coolant-Relative Model—defined features relative to the coolant trajectory in each case. This method allowed the Coolant-Relative Model to adjust to changing film conditions, making it more flexible than the Baseline Model.

Predictions of single-hole film-cooling flowrate were presented as the flow parameter ratio relative to the training case, and errors were quantified relative to the flow parameter ratio measured using a benchtop blade flow apparatus. The lack of flexibility for the Baseline Model resulted in a high prediction error for B4 of about 36%, while the Coolant-Relative Model resulted in a much lower prediction error of 7%. For the less extreme test cases (B2 and B3), slight increases in prediction error were observed when applying the Coolant-Relative Model, although the magnitudes of these changes were much lower than the improvement noted for B4. This observation suggests that the Coolant-Relative Model may be best applied only in scenarios when substantial changes to film-cooling have occurred, which can be determined directly from analysis of the IR images and subsequent comparison with the training case.

The models investigated in this study provide an important avenue for improving CBOM of gas turbine engines by enabling film-coolant flow monitoring during operation. Importantly, the same process shown in this study for a single film-cooling hole can be repeated for additional holes, enabling distributed flow monitoring across multiple areas on the blade. This information supports comprehensive monitoring of film-cooling hole degradation, meaning preventative maintenance can be executed prior to the occurrence of high-temperature blade failure. Additionally, when examining film-cooling flow variations in multiple regions of the blade, the distribution of ingested particulate matter can be inferred, which provides real-time feedback that can be applied to future designs. Altogether, the ability to monitor blade film-cooling flow enables engine manufacturers and operators to make more informed maintenance decisions, which supports the main goals of CBOM to reduce costs and increase engine availability.

## Acknowledgment

The authors would like to recognize Dr. Brian Knisely for his extensive work to develop and deploy the infrared imaging system utilized in this study. This material is based upon work supported by the Department of Energy under Award Number DE-FE0031288. The authors would also like to recognize and thank Pratt and Whitney for supporting the research presented in this paper.

This report was prepared as an account of work sponsored by an agency of the United States Government. Neither the United States Government nor any agency thereof, nor any of their employees, makes any warranty, express or implied, or assumes any legal liability or responsibility for the accuracy, completeness, or usefulness of any information, apparatus, product, or process disclosed, or represents that its use would not infringe privately owned rights. Reference herein to any specific commercial product, process, or service by trade name, trademark, manufacturer, or otherwise does not necessarily constitute or imply its endorsement, recommendation, or favoring by the United States Government or any agency thereof. The views and opinions of authors expressed herein do not necessarily state or reflect those of the United States Government or any agency thereof.

## Conflict of Interest

There are no conflicts of interest.

## Data Availability Statement

The authors attest that all data for this study are included in the paper.

## Nomenclature

$x$	= streamwise coordinate
$z$	= cooling hole pitchwise coordinate
$A$	= peak-to-trough effectiveness variation
$D$	= cooling hole diameter
$E$	= prediction error
$P$	= pressure
$S$	= pitchwise hole spacing
$T$	= temperature
$W$	= effectiveness peak width
$\dot{m}$	= mass flowrate
FP	= flow parameter
PR	= pressure ratio

## Greek Symbols

$\alpha$	= LASSO tuning parameter
$\beta$	= model coefficient
$\lambda$	= wavelength
$\Phi$	= array of cooling effectiveness features
$\phi$	= overall cooling effectiveness

## Superscripts and Accents

0	= training case
$BL$	= baseline model
$c$	= bulk blade coolant
$CR$	= coolant-relative model
$h$	= single-hole value
$in$	= inlet quantity
$meas$	= measured value
$MGP$	= main gas path
$nom$	= nominal condition
$out$	= outlet quantity
$pred$	= predicted value
$s$	= blade surface
$\bar{Q}$	= pitchwise-averaged quantity

## References

- [1] Bogard, D. G., and Thole, K. A., 2006, "Gas Turbine Film Cooling," *J. Propuls. Power*, **22**(2), pp. 249–270.
- [2] Koff, B. L., 2004, "Gas Turbine Technology Evolution: A Designer's Perspective," *J. Propuls. Power*, **20**(4), pp. 577–595.
- [3] Meher-Homji, C. B., and Gabriles, G., 1998, "Gas Turbine Blade Failures—Causes, Avoidance, and Troubleshooting," Proceedings of the 27th Turbomachinery Symposium, College Station, TX, pp. 129–180.
- [4] Crow, D. E., Tresa, P. M., Bradshaw, S., Foust, M. J., Graham, B., Gulen, J., James, A., et al., 2020, *Advanced Technology for Gas Turbines*, The National Academies Press, p. 5.
- [5] 2017, "Agilis," Agilis Measurement System Inc., <https://agilismeasurementsystems.com/>
- [6] Mathioudakis, K., Papathanasiou, A., Loukis, E., and Papailiou, K., 1991, "Fast Response Wall Pressure Measurement as a Means of Gas Turbine Blade Fault Identification," *ASME J. Eng. Gas Turbines Power*, **113**(2), pp. 269–275.
- [7] Kestner, B., Lieuwen, T., Hill, C., Angello, L., Barron, J., and Perullo, C. A., 2015, "Correlation Analysis of Multiple Sensors for Industrial Gas Turbine Compressor Blade Health Monitoring," *ASME J. Eng. Gas Turbines Power*, **137**(11), p. 112605.
- [8] Hee, L. M., and Leong, M. S., "Improved Blade Fault Diagnosis Using Discrete Blade Passing Energy Packet and Rotor Dynamics Wavelet Analysis," GT2010-22218.
- [9] Liu, J., Liu, J., Yu, D., Kang, M., Yan, W., Wang, Z., and Pecht, M. G., 2018, "Fault Detection for Gas Turbine Hot Components Based on a Convolutional Neural Network," *Energies*, **11**(8), p. 2149.
- [10] LeMieux, D. H., 2005, On-Line Thermal Barrier Coating Monitoring for Real-Time Failure Protection and Life Maximization, U.S. Department of Energy, DE-FC26-01NT41232.
- [11] Markham, J., Cosgrove, J., Scire, J., Haldeman, C., and Agoos, I., 2014, "Aircraft Engine-Mounted Camera System for Long Wavelength Infrared Imaging of In-service Thermal Barrier Coated Turbine Blades," *Rev. Sci. Instrum.*, **85**(12), pp. 124902-1–124902-7.
- [12] Jovanovic, M. B., de Lange, H. C., and van Steenhoven, A. A., "Influence of Laser Drilling Imperfections on Film Cooling Performances," Paper No. GT2005-68251.
- [13] Whitfield, C. A., Schroeder, R. P., Thole, K. A., and Lewis, S. D., 2015, "Blockage Effects From Simulated Thermal Barrier Coatings for Cylindrical and Shaped Cooling Holes," *ASME J. Turbomach.*, **137**(9), p. 091004.

- [14] Bunker, R. S. "Effect of Partial Coating Blockage on Film Cooling Effectiveness," Paper No. 2000-GT-0244.
- [15] Bogard, D. G., Schmidt, D. L., and Tabbita, M., 1998, "Characterization and Laboratory Simulation of Turbine Airfoil Surface Roughness and Associated Heat Transfer," *ASME J. Turbomach.*, **120**(2), pp. 337–342.
- [16] Wang, F. Q., Pu, J., Wang, J. H., and Xia, W. D., 2021, "Numerical Investigation of Effects of Blockage, Inclination Angle, and Hole-Size on Film Cooling Effectiveness at Concave Surface," *ASME J. Turbomach.*, **143**(2), p. 021007.
- [17] Sundaram, N., and Thole, K. A., 2007, "Effects of Surface Deposition, Hole Blockage, and Thermal Barrier Coating Spallation on Vane Endwall Film Cooling," *ASME J. Turbomach.*, **129**(3), pp. 599–607.
- [18] Barringer, M. D., Coward, A., Clark, K. P., Thole, K. A., Schmitz, J., Wagner, J., Alvin, M. A., Burke, P., and Dennis, R. "The Design of a Steady Aero Thermal Research Turbine (START) for Studying Secondary Flow Leakages and Airfoil Heat Transfer," Paper No. GT2014-25570.
- [19] Knisely, B. F., Berdanier, R. A., Thole, K. A., Haldeman, C. W., Markham, J. R., Cosgrove, J. E., Carlson, A. E., and Scire, J. J., 2021, "Acquisition and Processing Considerations for Infrared Images of Rotating Turbine Blades," *ASME J. Turbomach.*, **143**(4), p. 041013.
- [20] Mori, M., Novak, L., and Sekavčnik, M., 2007, "Measurements on Rotating Blades Using IR Thermography," *Exp. Therm. Fluid Sci.*, **32**(2), pp. 387–396.
- [21] Knisely, B. F., Berdanier, R. A., Wagner, J. H., Thole, K. A., Arisi, A. N., and Haldeman, C. W. "Effects of Part-to-Part Flow Variations on Overall Effectiveness and Life of Rotating Turbine Blades," Paper No. GT2022-83216.
- [22] Hassan, J. M., Mohamed, T. A., Mohammed, W. S., and Alawee, W. H., 2014, "Modeling the Uniformity of Manifold With Various Configurations," *J. Fluids*, **2014**, pp. 1–8.
- [23] DeShong, E. T., Peters, B., Paynabar, K., Gebraeel, N., Thole, K. A., and Berdanier, R. A., 2022, "Applying Infrared Thermography as a Method for On-line Monitoring of Turbine Blade Coolant Flow," *ASME J. Turbomach.*, **144**(11), p. 111009.
- [24] Tibshirani, R., 1996, "Regression Shrinkage and Selection Via the Lasso," *J. R. Stat. Soc. Ser. B*, **58**(1), pp. 267–288.